Investigation and Prediction of the Bending of Single and Tandem Pillars in a Laminar Cross Flow

Article *in* Journal of Fluids and Structures · July 2016

DOI: 10.1016/j.jfluidstructs.2016.07.017

4 authors:

Gabriel Axtmann
Universität Stttgart

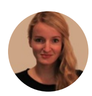

Franziska Hegner
Technische Universität Bergakademie Freiberg

Christoph Brücker
City, University of London

Ulrich Rist
Universität Stuttgart

Investigation and Prediction of the Bending of Single and Tandem Pillars in a Laminar Cross Flow

Axtmann G.[a,*], Hegner F.[b,], Brücker Ch.[c], Rist U.[a]

[a]*Institute of Aerodynamics and Gasdynamics, University of Stuttgart, Germany*
[b]*Institute of Mechanics and Fluid Dynamics, University of Freiberg, Germany*
[c]*Dept. of Mechanical Engineering and Aeronautics, City University London, UK*

Abstract

Cantilever beams are increasingly applied as sensory structures for force and flow measurements. In nature, such hair-like mechanoreceptors often occur not as single hairs but in larger numbers distributed around the body-surface and with different mechanical properties. In addition, reconfiguration of such structures with the flow changes their response and mutual interaction. This rises the question how it affects the signal conditioning on each individual sensor. Simple configurations involving single and tandem pairs of flexible cylinders (of aspect ratio 10) are studied as elementary units of such sensor arrays at Reynolds numbers of order Re_d=$\mathcal{O}$(1-10). Experimental reference studies were carried out with a tandem pair of up-scaled models using flexible cylinders mounted on a flat plate and towed in a viscous liquid environment. Direct numerical simulations (DNS) are used to determine the local drag along the rigid cylinders (pillars) for different orientations of the tandem relative to the main flow direction at steady flow conditions. The bending is then computed via beam bending theory. A prediction model based on the cross-flow velocity and an empirical relation for the drag coefficient is proposed and tested. The results show good agreement of the bending lines with the experiments and the direct numerical simulations for single and tandem configurations. It is then used to illustrate the expected sensor response at any point in a given complex flow field. This study contributes to the understanding of pre-conditoning effects in a sensor array measuring near-wall flow.

*Corresponding author: Axtmann@iag.uni-stuttgart.de (Axtmann)

Keywords: Micro-Cantilevers, Flow Sensors, Towing Tank, Experiments, Bending line, Direct Numerical Simulation, Timoshenko Beam Theory, Hairsensors

1. Introduction

Cantilevered beams and their interaction with the surrounding fluid in a low-Reynolds number environment became of interest with the invention of atomic force microscopy, where the beams act as sensors. The fluid-structure interaction is often of passive nature and studies have been carried out to determine the damping factor for the static and dynamic response of such sensors. Meanwhile, the technique has also been transferred to other disciplines such as aerodynamic measurements, where flexible micro-cantilever beams are attached to a surface to measure the distributed wall-shear stress WSS [1]. Therein, the latter acting on the beams is measured optically via imaging of the tip-displacement or using micro-electromechanical systems (MEMS) technology at their base.

In nature, such sensors occur as mechano-sensors in a wide range of different species [2]. To gain the information they need, animals have developed a stunning diversity of such hair-like sensors [3]. For example, fishes and aquatic amphibians use arrays of neuromasts along the lateral line systems and on the surface to detect minute water motions [4]. Other types of mechano-sensors are the filiform hairs, which are located on the cerci of crickets and enable the crickets to sense air movements generated by approaching predators [5]. Similar structures exist on the surface of the wings of a bat [3], [6]. It was found that these hairs are used by the bat to detect the flow pattern along the wing during their flight to enhance navigation and aerial manoeuvres like steep banking, hovering and landing upside-down [7]. This rapid detection of small-scale air-flow variations via the hair-shaft deflection of a single sensor or as part of distributed arrays contributes to natural flyers having greater flight agility than current engineering systems and is the inspiration for further investigations of such flow-sensing systems.

For a better understanding of the mechanisms of signal detection of such structures, standing either isolated or in arrays, a mathematical description of their response would be highly welcome, including the influence of the wall. For single shaft-hinged sensory hairs a model based on the Euler-Bernoulli/Timoshenko beam theory and Oseen's approximation for the viscous drag forces has been described in [8] and was later also applied to flexible micropillar-type WSS sensors [1]. A recent summary of the mathematical model of sensory hairs has been given in [9] and for flexible aquatic vegetation in [10]. These authors proposed a fluid-structure reaction model of the individual hair structure through a non-dimensional analysis of the hair model and they identified five non-dimensional parameters that directly determined the hair response. With this model they could simulate the response of a carpet of hairs along the circumference of a cylinder in cross flow. The results showed a time- and space-accurate representation of the surface flow patterns as long as the hairs are small enough. For the length of hairs considered (1/100th of the cylinder diameter), they found that the visualisation of the near surface flow topology was similar to the image of wall-shear-stress distribution. Therefore, wall-shear stress patterns can be detected via imaging of properly designed micro-pillars as demonstrated in [11]. However, these mathematical studies could not provide any insight into the effect of mutual interaction and coupling between sensors.

The purpose of the present work is to improve our understanding on the interaction of flow within an array of flexible structures of micro-scale for sensory application such as the flexible micro-pillars used for WSS imaging. To understand the complexity of the interaction a combined experimental and direct numerical simulation study has been performed. In experiments, largely up-scaled models of the hair sensors were built in the form of slender, wall-mounted circular beams of aspect ratio $h/d = 10:1$, where h is the length of the pillar and d the diameter, which bend under the action of the fluid forces in a towing tank system with a high-viscosity liquid. The cantilever beams were analysed in different flow conditions and configurations (single and tandem configuration) for the range of Reynolds numbers from 1 to 60 where vortex shedding is still absent. Additionally, Direct Numerical Simulations were carried out to investigate the rigid pillar-pillar interactions in the tandem configuration for different orientations in detail. Furthermore, a mathematical model of such flexible sensors is proposed, predicting the bending of arbitrarily placed sensors and estimating the sensitivity of the response signal by means of calculated bending lines.

2. Prediction model

The sensory structures considered in this study are the WSS sensors based on flexible silicone cylinders of micro-scale as described in [1]. Because of their small scale, the Reynolds number Re_d based on the diameter d of the sensor is typically in the order of $\mathcal{O}(10)$ or less:

$$Re_d = \frac{U_\infty d}{\nu}, \tag{1}$$

where U_∞ is the flow velocity at the sensor tip and ν the kinematic viscosity of the fluid. Direct numerical simulation (DNS) of a turbulent boundary layer containing a micro-sensor array with two-way fluid-structure coupling is still impossible because of the widely different scales between the sizes of the integration domain, the different size of eddies in the flow and the sensor diameters. This raises the question whether it would be possible to predict the bending of the sensors using a simplified model.

The basic idea for that is to consider a slender, wall-mounted cantilever beam of cylindrical cross section and finite length l which is treated as a one-dimensional Timoshenko beam in a two-dimensional, steady cross-flow boundary layer. The beam's drag can be estimated from the velocity of the cross flow and the beam's deflection then computed from Timoshenko beam theory:

$$EI\,\frac{\mathrm{d}^4 w(y)}{\mathrm{d}y^4} = q(y) - \frac{EI}{\kappa AG}\,\frac{\mathrm{d}^2 q(y)}{\mathrm{d}y^2}, \tag{2}$$

where y is the coordinate along the beam's length, E Young's modulus, I the moment of inertia, G the shear modulus, $q(y)$ the line load, $w(y)$ the bending line, and κ the shear rate coefficient ($\kappa = 0.9$). Young's modulus E and the shear modulus G are taken from the experimental data summarized in Tab. 1.

Our intention is to limit application of the present model to finite deflections from the vertical which could be used as a flow-sensor signal. For this, it is necessary that the sensor's tip remains within a limited distance from its base that can be resolved by some kind of optical measurement technique. Equally important is that the flow sensor does not leave the area of interest due to reconfiguration. In order to avoid extremely non-linear effects, the sensor should not be allowed to bend with the flow like a hair or a blade of grass.

A useful non-dimensional parameter for this constraint is the Cauchy number Ca, i.e., the ratio of drag force exerted by the fluid versus the restoring force of the beam due to stiffness. Following Luhar & Nepf [10], the Cauchy number is defined as:

$$Ca = \frac{1}{2}\frac{\rho_{fl} u^2 c_D d h^3}{EI}, \tag{3}$$

where ρ_{fl} is the density of the fluid, u the velocity and C_D the drag coefficient. It is clear that a beam will extensively curve with the flow if the load exerted by the drag force gets much larger than its restituting force. Therefore, for the present applications the Cauchy number must always remain limited. Investigations of the influence of Cauchy number on reconfiguration of plants are published in de Langre [12] and Luhar & Nepf [10], for instance. Especially the latter indicates that higher-order effects (which we don't consider here) slowly start after $Ca \geq 1 - 10$. Our worst case scenario will be shown in Figure 8 further down for Reynolds number $Re_d = 12$ and a maximal bending of $w/d \approx 7$ or $w/h \approx 0.07$ respectively. The corresponding Cauchy number is $Ca = 7$. A comparison with predictions of the present model shows that this case can be faithfully computed using our ansatz. To remain on the safe side, care is taken not to exceed $Ca = 7$ in the remaining investigations.

The higher fluid forces for larger Reynolds numbers can be easily compensated by a larger stiffness of the beam. As everything else is already fixed, this can only be done by changing the material properties, that is the elasticity modulus E. As a rule, E should be chosen according to the expected tip deflection, i.e. small for flows at small Reynolds numbers Re_d and large for large Reynolds numbers. This choice will guarantee that the sensor-tip displacement remains measurable in different applications without undue higher-order effects due to reconfiguration of the cylinder, like changes of cross section and orientation of bending line.

In contrast to a similar work by Jana *et al.* [13] the second-order theory (quasi-steady Timoshenko beam theory) used here takes changes in rotational inertia and shear deformation due to bending into account. Compared to linear Euler-Bernoulli theory it is more appropriate when structures are not slender anymore or if deflection gets large. Comparisons of first and second-order theory results with experimental results shown further down has confirmed the superiority of second order theory for the cases studied here.

The procedure for calculation of the bending line by a section-wise approach is sketched in Fig. 1. The line-load force $q(y)$ on the beam is then based on the standard ansatz

$$q(y) = c_d(y)\frac{\rho}{2}u(y)^2 d\, dy, \tag{4}$$

where ρ is the fluid density, $u(y)$ the local cross-flow velocity at the chosen y-position, d the pillar diameter, and dy the height of the considered section.

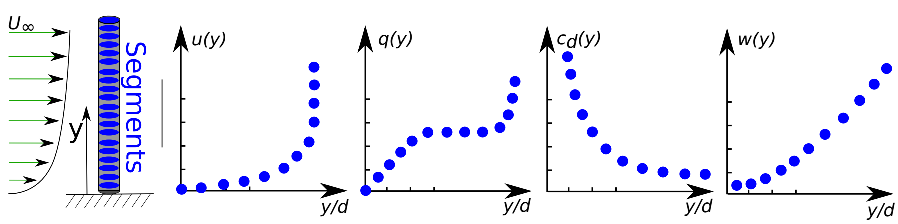

Figure 1: Sketch of cantilever beam in a cross flow $u(y)$, local drag force $q(y)$, local drag force coefficient $c_d(y)$ and resulting bending line $w(y)$.

In the following, we shall present an empirical formula for c_d as a function of local Reynolds number only

$$Re_{loc} = \frac{u(y)\, d}{\nu}. \tag{5}$$

The intention behind this proposal is to predict sensor signals (beam deflections) in spatially or temporally varying cross-flows solely on the basis of the unperturbed flow field. Of course, this is only possible if the diameter d of the beam is small compared to the relevant scales of the cross-flow, e.g., its boundary-layer thickness. The empirical formula will be established via direct numerical simulations (DNS) of flows around wall-mounted cylinders and validated by comparisons of the bending lines with experiments.

3. Model Validation

For validation of the above model towing-tank experiments and CFD simulations have been performed with up-scaled wall-mounted flexible cylinders, first for single cylinders, then for tandems. The experiment and the numerical set-up will be presented in the following subsections. In the following description we shall use the term 'rod' for the flexible cylinders in the experiment which bend and the term 'pillar' for the rigid cylinders in the numerical simulation because the latter are not allowed to bend. However, the bending of these simulated beams is computed via Timoshenko beam theory based on the actually obtained drag forces along the pillars' axes.

3.1. Experiments

The experiments were carried out in a transparent basin made of perspex (length: 3000 mm, depth: 250 mm, length: 400 mm) filled with a viscous working fluid, as shown in Fig. 2. On top of the basin is a traverse with a support cart that can be towed along the traverse up to maximum speeds of 1 m/s. A plate with a clamped beam is mounted on the support cart and immersed into the fluid. A high-speed camera records side views of the beam while the cart is towed. Images of the high-speed camera are then post-processed to determine the resulting bending line of the neutral fibre and the corresponding tip-bending.

The working fluid consists of pure glycerin to reduce the Reynolds number to the required low level. As glycerin is a hygroscopic fluid it is going to dilute

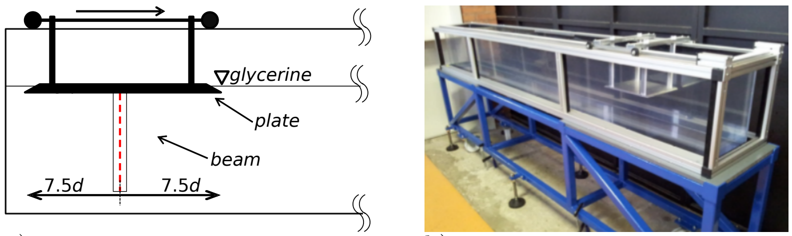

a) b)

Figure 2: Experimental setup of towing-tank experiments

with time. Therefore, prior to every run a fluid sample is taken from the tank and its current state of viscosity is measured.

The up-scaled models of typical wall-shear stress sensors are cast from silicone as flexible rods with a diameter of $d = 20$ mm and a free length in the fluid of $l = 200$ mm. Since silicone has a similar density as the working fluid, no significant buoyancy forces occur. These models are then clamped at one end to the wall of a flat plate with sharp leading edge that is towed along the open fluid surface in the tank. A colored thread marks the centerline of the rod to facilitate interpretation of the experimental bending lines. Material parameters and dimensions of the experiments are listed in Table 1.

Table 1: Material parameters and dimensions

Parameters	Dimensions	Parameters	Dimensions
Rod diameter d	20 mm	Elasticity modulus E	1.23 MPa
Rod length l	200 mm	Poisson ratio	0.3
Moment of inertia I	$7.85e^{-9}$ m^4	Shear modulus G	0.473 MPa
Aspect ratio l/d	10 : 1	Density ρ_{rod} of rod mat.	1030 kg/m^3
Dyn. viscosity glycerine	1 kg/ms	Density ρ_{fl} of fluid	1220 kg/m^3

Two typical experimental results for the single-beam configuration mounted in the center of the plate towed at different Reynolds numbers Re_d are shown in Fig. 3. For consistency with the simulation results further down these images were turned by 180°. As can be seen, the bending of the rod increases with increasing velocity. However, not in a linear manner.

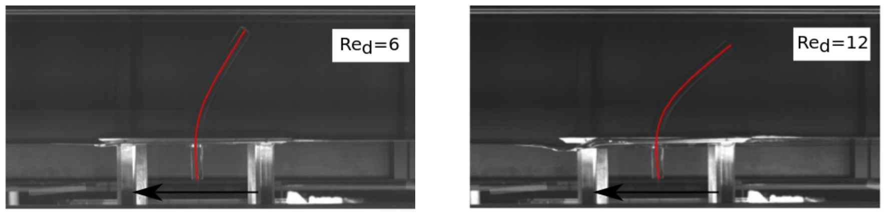

a) b)

Figure 3: Bending lines of single flexible rods in experiment at two different Reynolds numbers

3.2. Numerical Simulation

For solving the Navier-Stokes-Equation, the CFD toolbox OpenFOAM is used. Due to the low Reynolds numbers, a laminar viscous fluid model is chosen, resulting in a DNS simulation. In contrast to the experiment the numerical model considers rigid beams, i.e., *no* fluid-structure interaction. To distinguish these non-flexible structures in DNS from the flexible ones in the experiments we name the former 'pillars' instead of 'beams' or 'rods'. The purpose of the DNS is to provide the fluid force distribution along the pillar which is not accessible in the experiments. These forces are then used as a line-load profile $q(y)$ in equation (2) for prediction of the pillar's bending line under load, cf. Fig. 1. In addition, the DNS leads to additional insight into the three-dimensional flow field around the pillars.

The integration domain for the numerical simulation is presented in Fig. 4. As the coordinate system of the simulation is fixed to the moving plate with surface-mounted pillar, the towing tank transforms to a channel with rectangular cross section. A boundary layer develops at the leading-edge of the flat plate, as in the experiment. All dimensions and parameters are chosen to simulate the experiments as close as possible. For an efficient simulation the lateral sides of the domain, the top wall and parts of the bottom are implemented as slip walls. The ground plate and the pillar itself are defined as a friction wall. Inlet and outlet conditions are set to freestream and zero-gradient conditions, respectively. In single-beam configuration, the pillar is mounted in the center ($7.5d$) of the plate.

A structured mesh is used to discretize the flow field around the pillar.

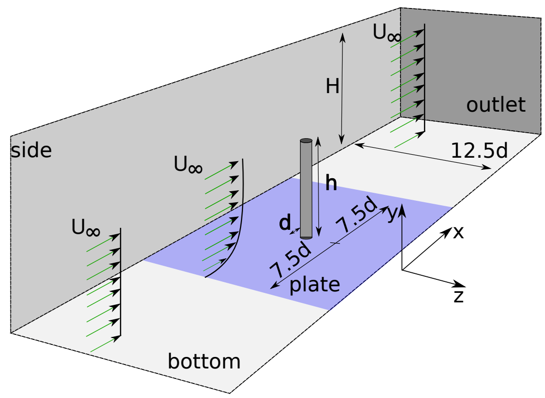

Figure 4: Computational domain to simulate towing tank experiments. Blue area represents ground plate towed through tank together with cylindrical pillar.

Equidistant wedge elements are used around the pillar and the cross-flow boundary layer resolution uses around 60 elements. In the far field Cartesian grids are used and the finite end at the top of the pillar is closed by a butterfly mesh. To avoid high aspect ratios in tandem configurations, a hybrid mesh approach is applied then. A grid convergence study following Roache [14] was conducted to evaluate discretization errors with determination of the Grid Convergence Index (GCI). The error stays within an error band of 0.5 %.

For calculation of the bending line the local drag forces $F_{loc}(y)$ acting on the pillar's surface are needed. For this purpose the pillar is subdivided into individual disk-like segments of length dy in y-direction, cf. Fig. 1. The local force is then extracted from the DNS data for each slice at $y = const.$ according to

$$q(y) = \int_S (p(y) - p_\infty)\, \hat{n} \cdot \hat{i} dA + \int_S \tau_{w_{xz}}(y)\, \hat{t} \cdot \hat{i} dA, \tag{6}$$

where $p(y)$ is the local pressure, p_∞ the ambient pressure, $\hat{n}$ the vector normal to the surface, $\tau_w(y)$ the local wall shear stress, $\hat{t}$ the tangent vector, $\hat{i}$ the unit vector, $dA = d \cdot dy$ the projected area normal to the flow, and S the surface integral of the segment. Determining the local pressure, the Semi-Implicit Method for Pressure-Linked Equations (SIMPLE) which comes with OpenFOAM is used. It allows coupling of the Navier-Stokes equations with an iterative procedure correcting the velocity on the basis of the newly calculated pressure field in a fractional manner.

The ratio of the pressure drag coefficient $\overline{C_p}$ to friction drag coefficient $\overline{C_f}$ integrated over the pillar's length l is given in Tab. 2. While for $Re_d = 1.0$ the ratio of $\overline{C_p}/\overline{C_f}$ is 1.09 it increases with higher Reynolds numbers in a non-linear manner up to 2.26 for $Re_d = 60$. Here, the pressure drag coefficient $\overline{C_p}$ gets more dominant while the friction drag coefficient $\overline{C_f}$ decreases.

Table 2: Change of drag ratio ($\overline{C_p}/\overline{C_f}$) with Reynolds number

Re_d	1.0	6.0	12.0	60.0
$\overline{C_p}/\overline{C_f}$	1.09	1.22	1.39	2.26

For comparison with literature the mean drag coefficient $\overline{C_D} = \overline{C_p} + \overline{C_f}$ of the pillar is computed via

$$\overline{F_D} = \int_0^l q(y)\,dy \tag{7}$$

$$\overline{C_D} = \frac{2\overline{F_D}}{\rho U_\infty^2 l \cdot d}, \tag{8}$$

where $\overline{F_D}$ is the total drag force acting on the pillar in streamwise direction.

As shown in Fig. 5, the DNS results for the global drag coefficient $\overline{C_D}$ compare well with the empirical drag-coefficient curve for circular cylinders in two-dimensional flow (Tritton [15]). For Reynolds numbers below $Re_d \approx 10$ the drag coefficient is somewhat larger than this reference while it is lower for $Re_d > 10$. The present DNS results are well confirmed by the towing-tank experiments in the range where experimental results are available. The curve fit of Jana *et al.* [13] is intended to provide an improved estimation for the global drag coefficient $\overline{C_D}$ of slender cantilever beams in a cross-flow in the range of $1 \leq Re_d \leq 63$ to Tritton's empirical ansatz. Their curve is shown in Fig. 5 as a green dashed line. Still, a slight offset of Jana *et al.*'s fit to the present results is observed. However, this can be corrected by using different constants compared to those given in [13], see equation (9).

$$\ln \overline{C_D} = 2.71 - 0.80\,\ln(Re_d) + 0.06\,\ln(Re_d)^2 \tag{9}$$

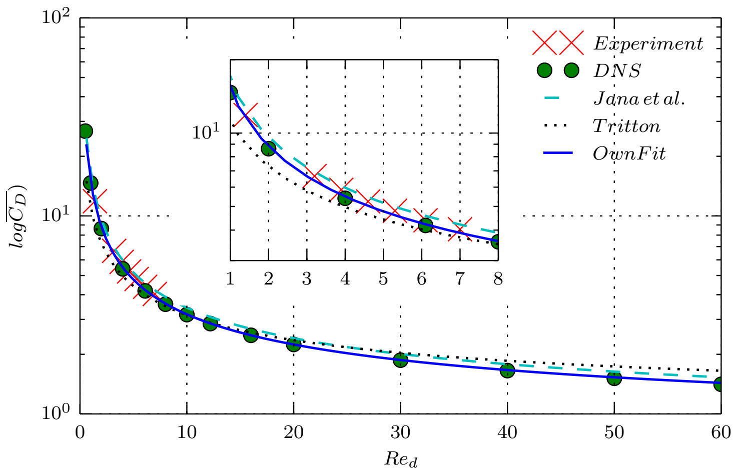

Figure 5: Comparison of global drag coefficient $\overline{C_D}$ versus Reynolds number Re_d between simulation (DNS), experimental data (X), literature, and own fit.

The new fit meets the numerical results within the range of $1 \leq Re_d \leq 63$ nearly perfect. It will be used to model $c_d(y)$ as a function of local Reynolds number Re_{loc} for prediction of beam-bending using the model described in section 2, i.e.,

$$\ln c_d(y) = 2.71 - 0.80\,\ln(Re_{loc}) + 0.06\,\ln(Re_{loc})^2. \tag{10}$$

Beforehand, however, we shall compare this formula to actually obtained drag coefficients in Fig. 6 and discuss those effects which are responsible for differences of the present flow field with respect to two-dimensional flow around a circular cylinder.

The *local* drag coefficients $c_d(y)$ have been computed from $q(y)$ via inversion of eqn. 4 and compared with eqn. 10 for four representative cases with different Reynolds numbers Re_d. The primary effect of the Reynolds number is that the cross-flow boundary layer becomes thinner with increasing Re_d such that the part of the pillar that protrudes the boundary layer becomes larger for increasing Re_d. This leads to constant $c_d(y)$ versus y in Fig. 6, especially for $Re_d = 60$. Despite the fact that the modeled $c_d(y)$ is based on the mean drag, there is an excellent agreement of c_d in the free-stream for all Reynolds numbers. Modeled and real curves do not fully agree within the cross-flow boundary layer and directly at the pillar's tip. The mismatch at the tip is clearly insignificant and the mismatch at the bottom depends on Reynolds number. Fortunately, a larger quantitative difference in the large-Reynolds-number case is compensated by a smaller extent of the boundary layer there, while the quantitative difference is less severe for the smallest Reynolds number where the boundary layer stretches almost over the complete length of the pillar. The ratio of δ_{99}/h, where δ_{99} is calculated by the laminar boundary layer solution of Blasius and h the length the pillar, is given for $Re_d = 1, 6, 12$ and 60 in Table 3. Jana *et al.* [13] mentioned already that tip effects can be faithfully neglected because they lead to a deviation of less than 5 % for the tip bending.

Table 3: Ratio of boundary layer thickness δ_{99} and length h of pillar with respect to Reynolds number

Re_d	1.0	6.0	12.0	60.0
δ_{99}/h	1.34	0.54	0.38	0.17

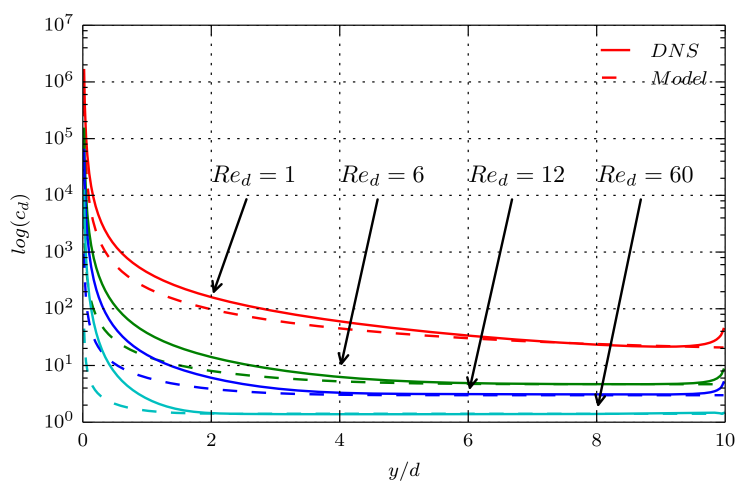

Figure 6: Comparison of local drag coefficients c_d between direct numerical simulation (DNS) and model (eqn. 10) for Reynolds number $Re_d = 1, 6, 12$, and 60.

A closer look at the flow around the pillar is presented in Fig. 7 for $Re_d = 6$

and 40. For low Reynolds numbers $Re_d \leq 10$, the flow field in the upstream part of the pillar is dominated by a down-wash effect near the bottom wall which bends the streamlines near the pillar down to the wall and leads to a three-dimensional flow structure. This effect decreases with higher Reynolds numbers. Between the region of high velocity gradients at the wall and the tip a quasi two-dimensional flow regime is observed. A typical up-wash effect of the flow near the tip occurs as well. The pillar's tip generates high velocity gradients and accelerates the fluid locally. The lee-side of the pillar is characterized by an up-wash effect from the wall towards the tip, whereas a weak down-wash near the tip is seen.

For higher Reynolds numbers, a significant increase of the rear-side effects is observed, as seen in Fig. 7b) for $Re_d = 40$. Additionally, a steady separation bubble appears along the pillar's length on the rear-side and a huge down-wash starts from the tip. The latter one leads to higher velocity gradients of the flow further downstream in the wake of the pillar. These flow features are also observed in experiments as shown in Fig. 7c), which exhibits an excellent agreement of the flow patterns observed in DNS (Fig. 7d).

4. Results

4.1. Single-Beam Configuration

A comparison between measured and calculated bending lines is presented in Fig. 8 for $Re_d = 6$ and 12. Bending lines calculated from the DNS *with* pillars are shown as solid lines whereas the modeled load profiles using the correlation given in equation (10), where Re_{loc} is calculated from the undisturbed cross-flow velocity, i.e., a DNS *without* pillars is marked with filled circles. These curves are in excellent agreement with each other and also with the experimental results ($\times$). This shows that both, DNS-based bending lines and modeled bending lines can be used for further investigations.

Fig. 9 shows further comparisons of results using the prediction model with results based on the actual drag forces from DNS for the complete range of

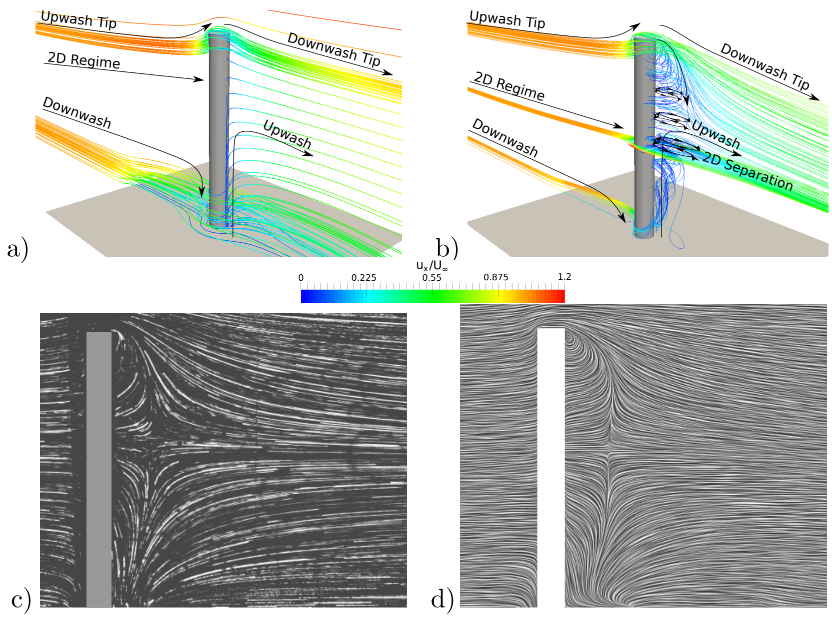

Figure 7: Visualisation of three-dimensional flow features for a) $Re_d = 6$, b) $Re_d = 40$, c) experimental flow visualisation and d) Line Integral Convolution (DNS) for $Re_d = 30$

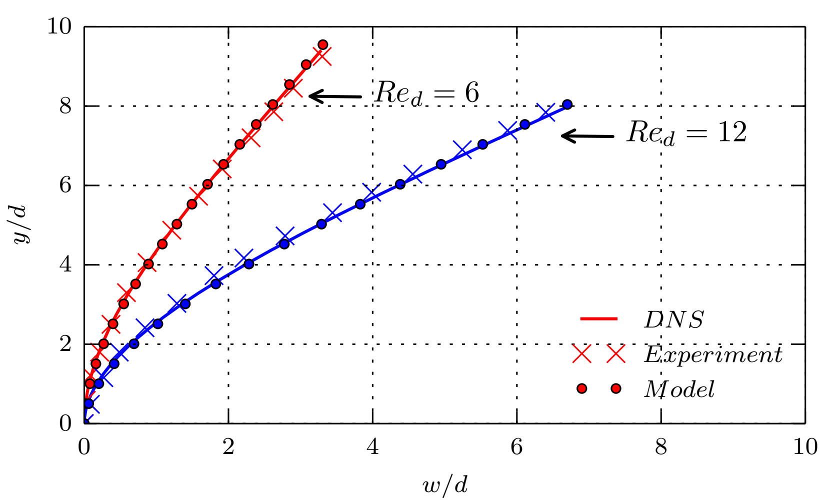

Figure 8: Comparison of bending lines w/d from experiments ($\times$), direct numerical simulation (—–) and model prediction ($\circ$) for $Re_d = 6$ and 12. Note that horizontal axis is stretched with respect to vertical one for visualisation purposes.

investigated Reynolds numbers $1 \leq Re_d \leq 60$.

As discussed above Young's modulus E has been increased for these investigations by a factor of 100 with respect to the value given in Table 1 in oder to keep the Cauchy number below 7.

The maximum relative difference at $y = 10d$ is less than 3.9 % for all Reynolds numbers. These deviations are caused by neglecting tip effects within the prediction model, as shown in Fig. 6. The relative error is largest for the smallest Reynolds numbers in agreement with the difficulties of fitting a universally valid drag curve through the data of Fig. 6 with equation (10). As a result, a non-linear connection between tip deflection and Reynolds number is observed. Due to the fact that the drag coefficient decreases while the force increases with the velocity, the tip deflection w_{tip} increases with Re_d. The present results indicate that the tip displacement scales to the power of 1.6 with respect to Re_d in the investigated range of $1 \leq Re_d \leq 60$.

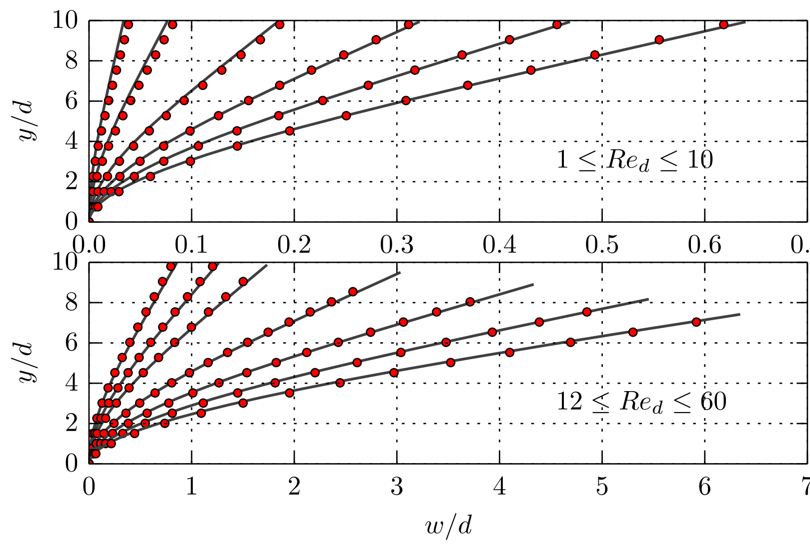

Figure 9: Comparison of bending lines w/d from prediction model (○) with those obtained by using the drag from direct numerical simulation with pillars (——) for $Re_d = 1$ to 60. Elasticity modulus E scaled by factor 100. Note that horizontal axis is stretched with respect to the vertical one for visualisation purposes.

4.2. Tandem-Beam Configuration

The previous section showed that the introduced prediction model is able to predict the bending of an isolated slender rod in a boundary layer cross-flow reasonably well. Our next step now will be to evaluate if the model can be used to predict the bending of a second beam that is positioned at some distance to the first one as well. The motivation for this investigation is based on the need to quantify interaction effects of sensors which are arranged in an array. Using two beams is the basic element of such an array and a method for easy quantifications of mutual interactions would be very valuable for the design of sensor arrays.

A slight modification of the experimental and numerical setup has been performed compared to Fig. 2 and Fig. 4. Now we consider two rods that are towed through the tank, see Fig. 10. The first rod (termed 'luv') is positioned at a distance of $2.5d$ from the leading edge of the flat plate and the second rod (termed 'lee') at a distance of $10d$ from the first. The center of the coordinate system is still in the middle between both rods for reference. Experiments with this tandem configuration were limited to lower towing speeds $U_\infty \leq 0.3\ m/s$ because the tandem generates a larger disturbance in front of the plate that modifies the inflow conditions. For comparison with the direct numerical simulations, the case with $Re_d = 6$ is taken as reference.

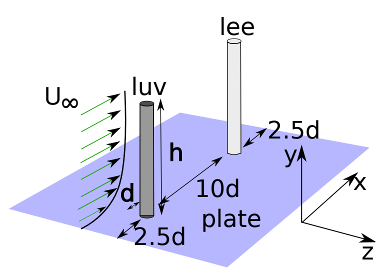

Figure 10: Model modification used for tandem-beam configuration

In experiment both flexible rods bend with the flow. As before, our ability to simulate this in CFD is restricted to flows without fluid-structure interaction, i.e., rigid pillars. The influence of the luv pillar on the lee one will be estimated first. For this, two simulations have been compared. One where both pillars are straight and normal to the plate and one where the luv pillar is bent towards the lee one according to the bending line predicted by our model.

Flow field visualisations of both cases are shown and compared in Fig. 11a)+b). It can be seen, that the bending (reconfiguration) of the first beam leads to a stronger up-wash effect of the streamlines on its rear side. A slight increase of the axial velocity near the tip area is observed as well. Comparing the spatial development of the wake behind the luv beam of the vertical relative to the bent configuration, a streamlining effect is observed, as shown in Fig. 11c)+d). The bent configuration leads to higher curvature of the flow along the pillar‘s length. Yielding a more streamlined shape of the luv beam, the overall drag decreases up to 11 % relative to the vertical one.

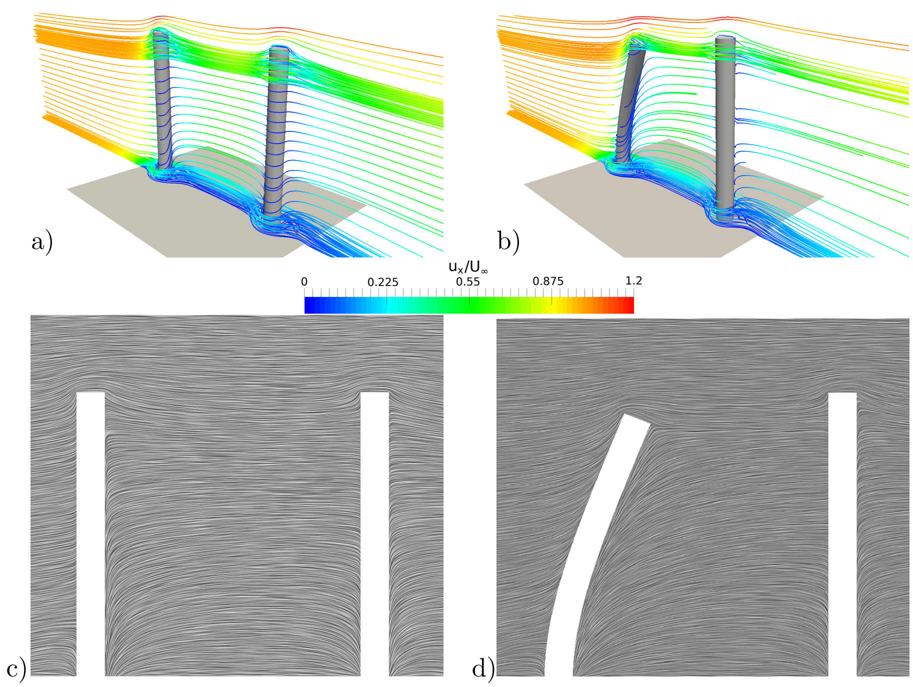

Figure 11: Flow field of tandem configuration a) first pillar vertical, b) first pillar bent, c) first pillar vertical (LIC) and d) first pillar bent (LIC)

However, as shown in Fig. 12, this does not affect the resulting bending line of the lee pillar significantly. The expected tip bending of the lee beam is only slightly lower in case of a pre-bent luv pillar compared to the case with a straight first pillar.

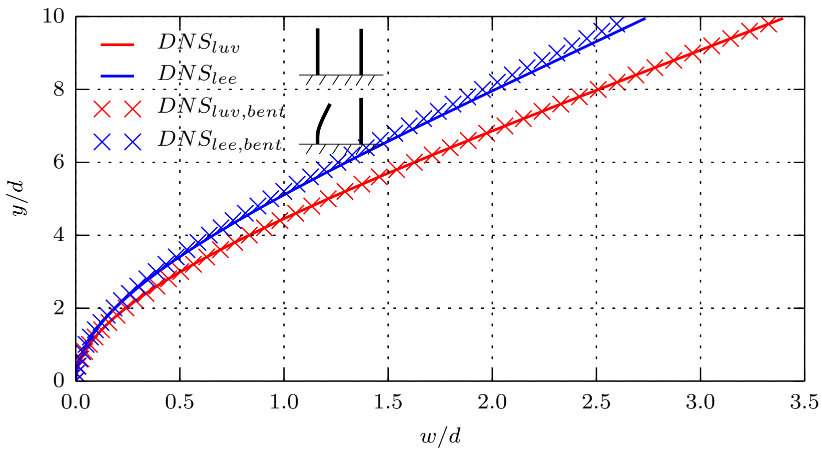

Figure 12: Comparison of bending lines of first and second beam for two different shapes of the luv pillar at $Re_d = 6$. Note that horizontal axis is stretched with respect to the vertical one for visualisation purposes.

Fig. 13 shows the two rods mounted in tandem configuration for the present setup in the experiment. For reference the corresponding image without cross-flow is shown as well ($Re_d = 0$).

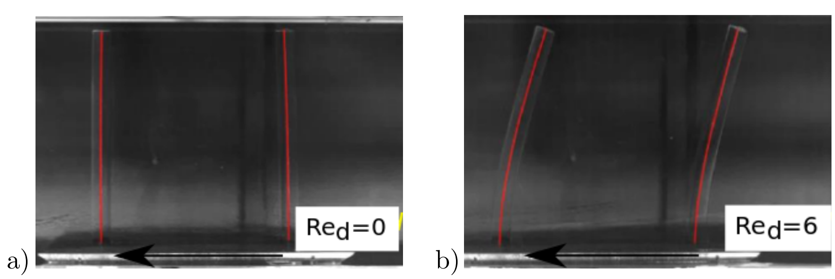

Figure 13: Experimental results of inline tandem configuration (a) at rest and (b) for Re_d. The black arrows indicate the towing direction during experiments.

The luv beam always bends more than the lee one, because it receives the full load of the cross-flow while the lee beam is in the wake of the luv, see Fig. 14.

The beam bending lines of the DNS (——) are obtained by integration of the actual forces of each pillar in a simulation of the full tandem configuration. In contrast to this, the prediction model uses either flow-field data from a simulation without any pillar for prediction of the luv beam or data from a simulation with the luv pillar only for prediction of the lee beam. Apparently, our model performs remarkably well for both beams. Experimental results are also in close agreement for both beams with the theoretical predictions.

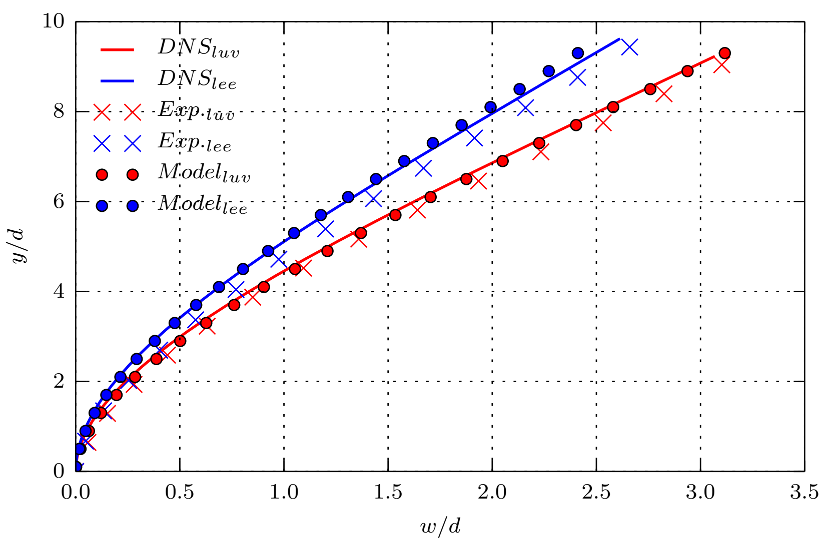

Figure 14: Comparison of bending lines w/d between experiments ($\times$), DNS (——) and model estimation ($\circ$) for $Re_d = 6$. Note that horizontal axis is stretched with respect to vertical one for visualisation purposes.

4.2.1. Influence of Distance and Position

Now, the bending of a second beam in the wake of a first one is investigated for various relative positions. In the experiment, the lee rod is placed at a fixed distance relative to the luv rod on the plate but at different angular positions, see Fig. 15a). The polar angle φ is varied in equal steps between $\varphi = 0^o$ and 30^o.

The color contours of $\Delta u = u - U_\infty$ from the DNS flow field with a single pillar at the position of the luv beam in Fig. 15a) visualise the influence of the first pillar on the surrounding flow field at a typical y-position. The flow field resembles the flow around a two-dimensional circular cylinder with a velocity decrease in the stagnation area, areas of increased velocity on the sides of the pillar, and a Reynolds number dependent wake. It is clear that placing a second beam in the flow field of the first one will lead to lower or higher deflection of the second depending on its load which is a function of the velocity profile. This expectation will be quantified further down with the beam-deflection model presented above. Beforehand, we present the same validation steps for the tandem case as before for the single pillar setup.

DNS simulations containing two pillars were carried out, the drag forces along the pillars were extracted for integration of bending lines to obtain the relative bending at the beam's tip w_{tip}/d. Fig. 15b) compares these results for both beams with those for the single beam. The just mentioned expectation that the lee beam experiences a large variation of its tip deflection depending on its spanwise position is clearly evident. Interestingly the luv beam is deflected less than the single beam in those cases where the lee beam is within the wake of the first. This means that there is a slight upstream effect of the lee beam.

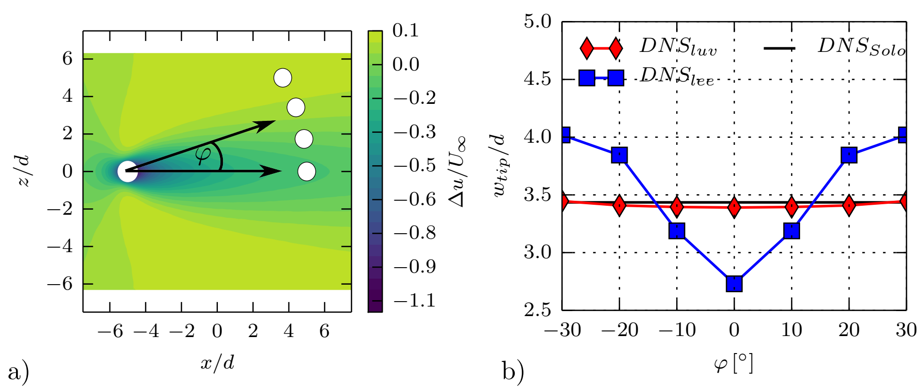

Figure 15: Investigation of interaction effects. a) Normalized velocity difference due to one pillar together with investigated positions of the second. b) Computed maximal bending at tip of different beams w_{tip}/d

Figure 16 presents the actually obtained flow fields for different positions of the lee-ward pillar in the DNS. The colour contours visualise velocity defects (blue) and velocity excess (yellow) with respect to the undisturbed cross-flow (without pillars). The figure series a) to d) nicely illustrates how the flow field changes when the second pillar leaves the wake of the first. At $\varphi = 0^o$ the lee-ward pillar is fully in the wake of the first and the flow field is symmetric. At $\varphi = 10^o$ the second pillar is still within the reduced velocity due to the wake of the first and hence experiences less drag. At $\varphi = 20^o$ and 30^o the luv pillar's wake disturbs partly still the inflow of the lee pilar, such that the latter encounters velocity excess due to fluid displacement around the first pillar which leads to a higher drag force and hence larger bending of the lee beam.

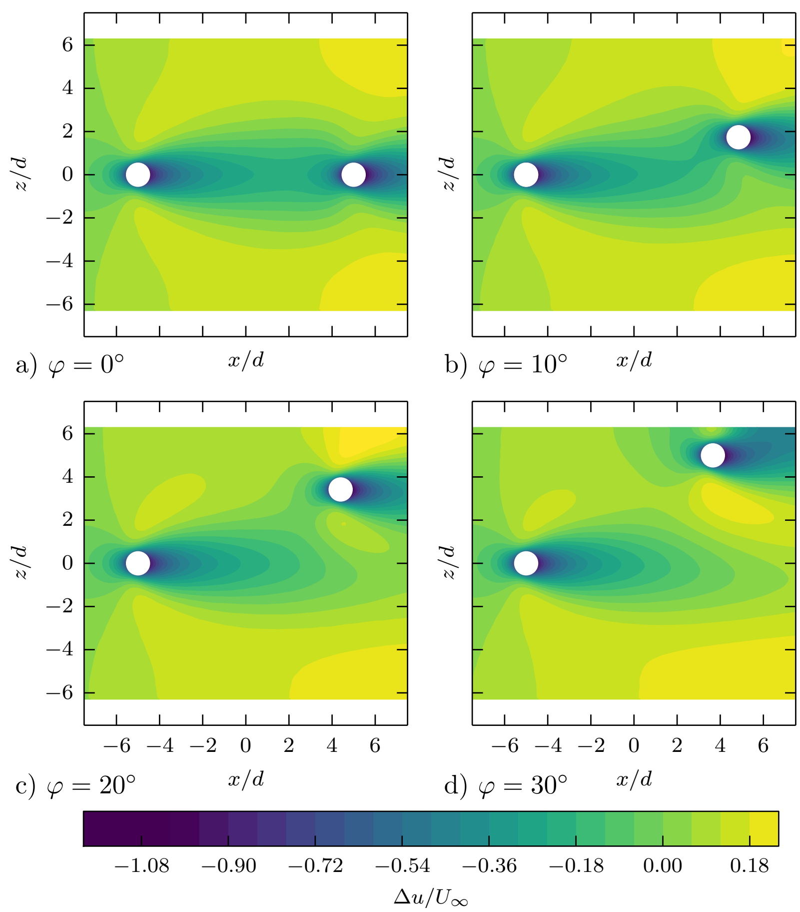

Figure 16: Normalized velocity differences $\Delta u/U_\infty$ for tandem configuration from DNS at $y = 10d$

4.3. Examination of model prediction

The main purpose of the model described in section 2 is to obtain predictions of sensor output signals (i.e., beam deflection at the sensors' tips) for laminar or locally averaged flow fields at minimum effort, such that an existing DNS flow field can be mapped out by fictive sensors placed at any position in the flow. This procedure can be applied and tested for the present tandem-pillar setup using a flow field that contains only one pillar. According to the model the velocity profiles $u(y)$ are extracted along a line above a point (x, z) starting from the ground plate until $y = l$, transferred to Re_{loc} via equation (5), then to $c_d(y)$ via equation (10) followed by $q(y)$ to finally yield $w(y)$. Results for the maximal bending at the tip of the beam are shown in Fig. 17 both as color contours in Fig. 17a) and as lines in Fig. 17b). These values can be compared with w_{tip}/d at those positions where experimental and DNS results are available from the simulations used for the previous section. It turns out that the model predictions are in surprisingly good agreement with the full simulations and experimental results, however, at almost no extra costs because one DNS containing one pillar is sufficient for the model. This is in strong contrast to the full DNS, which needs a new grid and an extra simulation run for each pillar position. Apparently, our model estimates the tip bending of the lee beam for the investigated angle range between $-30^o \leq \varphi \leq 30^o$ remarkably well. The maximal relative difference of the prediction model to DNS is ≈ 3.7 % and of the experiments to DNS ≈ 6.0 %.

The prediction model is now used to quantify the mutual influence of the two pillars via changes in the flow field. For this the relative tip displacement with respect to a beam sensor in the undisturbed cross-flow is used:

$$w_{rel} = \frac{(w - w_{FlatPlate})}{w_{FlatPlate}} * 100 \ [\%], \tag{11}$$

where w is the tip displacement in the presence of a pillar, and $w_{FlatPlate}$ the corresponding value for flat-plate boundary layer flow without pillar. Since the amplification factor of the bending scales by the power of 1.6 in relation to the Reynolds number, a much clearer presentation of the raising effects to the bending than to the velocity can be obtained in Fig. 18 and Fig. 19. This

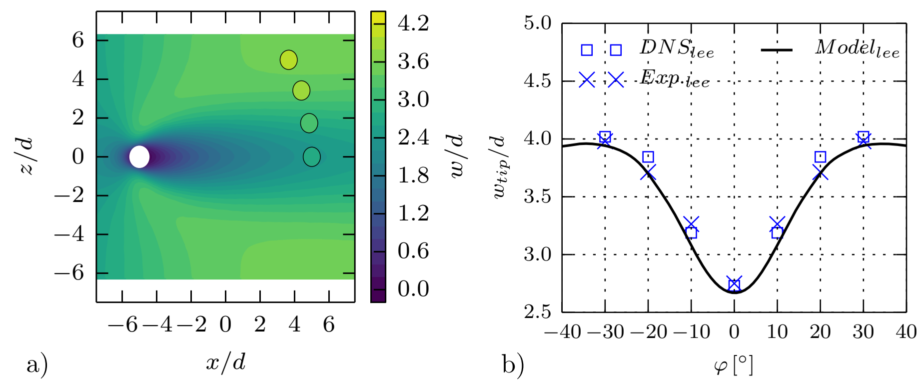

Figure 17: Comparison of model prediction for tip bending w_{tip}/d with tip bending obtained from DNS data at discrete lee-ward pillar positions.

relationship is a useful sensitivity metric for designing sensor arrays in order to maximize the bending at the tip by varying the elasticity modulus E or the diameter d for Cauchy numbers $Ca \leq 10$.

Results are visualised in Fig. 18 in such a way that the mutual influence of one beam on the other is emphasized. Extra bending due to velocity excess with $w_{rel} > 0$ and reduced bending due to velocity defects $w_{rel} < 0$ are shown in red and blue, respectively. The neutral line $w_{rel} = 0$ is found in the contour lines. Fig. 18a) is based on the DNS flow field of the first pillar alone, while subfigure b) uses the flow field for the second (lee) pillar alone. In Fig. 17b) a subset of the data shown in Fig. 18a) has already been discussed. According to the iso-line values, the influence of one pillar on the sensor signal of a second one can be quite large, ranging, for instance from -40% in the immediate wake to $+25$ % to the side and slightly behind the first (see contours). If the CFD simulation were continued beyond the extent of the flat plate from the towing tank experiment, i.e., beyond $x/d = 7.5$, one could observe where the isoline $w_{rel} = 0$ returns to $z = 0$ thus ending the domain of influence. Since this would be very far downstream it is much better to use iso lines $w_{rel} = const$ to identify those areas where the influence exceeds or stays below a certain threshold. These lines are already given here.

In Fig. 15b) a reduced bending of the luv beam has been observed due to an upstream influence of the lee one. Whether this effect would be due to an upstream influence of the second pillar alone can be evaluated from the iso-contours in Fig. 18b). There is indeed a reduced area of displacement due to the stagnation area in front of the second pillar. However, as the contour line $w_{rel} = 0$ does not reach $x/d = -5$ such a trivial effect can be excluded via the model. Thus, both cylinders interact in a non-linear manner when their domains of influence interfere. This is not accounted for by the prediction model but the model is very fast and the prediction errors appear acceptable for those positions where such non-linear interactions are not dominant. A distance of 10 diameters is already sufficiently large for the model to be valid according to the comparisons with the full DNS in the previous subsection.

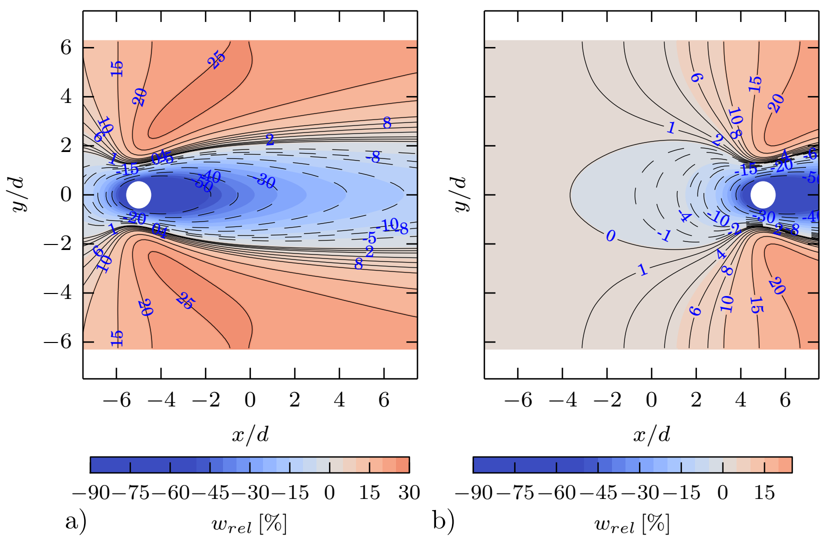

Figure 18: Model predictions of relative bending w_{rel} of a virtual sensor beam for a) first beam at frontal position (luv) and b) beam at rear position (lee).

4.4. Examination of Tandem Beam Configurations

The results of the previous subsection have shown how the prediction model can be used for mapping of complex flow fields by placing a virtual beam-sensor probe at any position in a given flow field. This possibility is further illustrated in Fig. 19 where the four DNS flow fields already shown in Fig. 16 containing two pillars have been used. The already introduced iso lines and colour contours give a clear overview of increased and decreased bending due to local velocity increases and defects. Much clearer than the colour contours in Fig. 16.

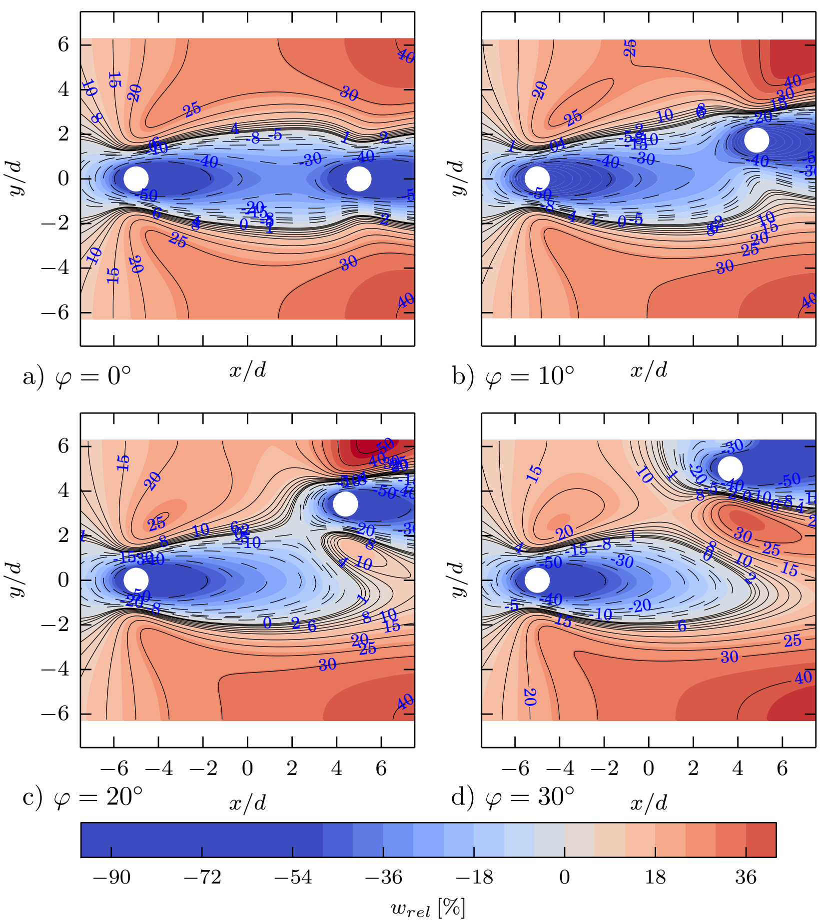

Figure 19: Model predictions of relative bending w_{rel} for flow fields containing two pillars.

5. Conclusions and Outlook

A prediction model of bending of flexible wall-mounted beams in a boundary layer flow is presented. This is an update of the prediction model published by Jana *et al.* [13] as it differs firstly, by the use of second-order Timoshenko beam theory and secondly, by the slightly modified constants for the empirical correlation of the drag coefficient with Reynolds number that take herein into account the wall-effect. The model has been successfully validated with respect to towing-tank experiments of up-scaled beams (flexible rods) and numerical simulations of the flow around rigid cylinders (pillars).

Such wall-mounted flexible beams can be used to probe a flow field with the tip deflection of a beam as sensor-signal output. Using the computed flow field around one pillar a fictive beam has been employed to investigate the interaction effects of two sensors as a basic element of a sensor array. These interaction effects are mainly caused by local changes of the flow field due to the presence of a sensor which leads to areas of velocity defects and excesses compared to the undisturbed flow. If another sensor happens to be in these areas its signal output is either accordingly decreased or increased. When the signal output is expressed as the relative error to a sensor in the undisturbed cross-flow, these influences can be clearly visualised with the prediction model as a second sensor. Areas of increased and decreased sensor-signal output have been mapped out by this method for flow fields with two pillars at different relative positions as well.

Some interesting conclusions with respect to using sensor tandems as improved flow sensors can be drawn from the present results: if the two sensors are placed at a certain distance from each other along the mean flow direction, like $10d$ as suggested here, then the luv sensor is not much affected by the presence of the lee one and its signal can be used as a reference for the other. Normally, the luv signal falls below the lee signal since the lee sensor is in the wake of the luv. As lateral flows appears, it may happen that the lee signal gets higher as it comes into areas of high-speed fluid that surround the luv wake.

A calibration could be derived from results like those shown in Fig. 17b) such that the sensor pair can be calibrated to measure the yaw angle of mean flow direction relative to the axis of the tandem. The velocity magnitude is still obtained via the tip displacement of the luv sensor. The directional sensitivity of a sensor pair could also be exploited by combining a single sensor with a passive structure (e.g., a rigid pillar) in its luv, such that the sensor is in the wake of the obstacle in the reference position. Then, if sidewinds occur such that the lee sensor leaves the wake, there will be a large increase of sensor signal which is much easier to detect than changes of flow direction using a single sensor element alone. A rough estimate yields a three-times higher sensitivity of such a tandem pair against a single sensor regarding the detection of yaw angle. These effects could probably be used to construct sensor arrays which are optimized for detecting certain flow events. An according investigation has already been performed using a modification of the towing-tank setup presented here. Results of these investigations will be published in a separate article.

The prediction model has been validated here for cross flows with a boundary layer thickness in the order of the sensor length l. In future we shall return to applications where such sensors are applied to measure instantaneous wall-shear stress fields and detect wall-events in turbulent flows. For that purpose the sensors will have lengths in the order of the thickness of the viscous sublayer and they will encounter velocity profiles similar to plane Couette flow. For that purpose the prediction model must be re-calibrated for plane Couette flow. Earlier practical applications of flexible micro-pillars in turbulent boundary layers as WSS sensors have already used plane Couette flow for calibration of the tip displacements with respect to the wall shear stress magnitude, cf. [1]. Using the prediction model together with DNS of the investigated flows will be helpful to understand the connection of near-wall events and wall shear signals. The model will then be used to device sensor arrays which 'fire' when a specific event occurs. Such information is important for flow control if a control actuator is to be used that is optimized for such an event. The idea behind this concept is similar to the situation in biology where a predator senses his prey in complete darkness solely on the basis of optimized, sudden sensor signals which might come from specifically designed and arranged sensor hairs on his skin.

6. Acknowledgements

Part of this study was funded by the DFG (Deutsche Forschungsgemeinschaft) under reference numbers BR 1494/25-1 and RI 680/28-1. This funding is gratefully acknowledged herein. Ms. Hegner was also funded for three months by the Air Force Office of Scientific Research, Air Force Material Command, USAF under Award No. FA9550-14-1-0315 and program manager Russ Cummings. Funding of the position of Professor Christoph Bruecker as the BAE SYSTEMS Sir Richard Olver Chair in Aeronautical Engineering is gratefully acknowledged herein.

References

[1] C. Brücker, J. Spatz, W. Schröder, Feasability study of wall shear stress imaging using microstructured surfaces with flexible micropillars, Experiments in Fluids 39 (2) (2005) 464–474. doi:10.1007/s00348-005-1003-7.

[2] T. W. Barth, F.G.; Humphrey, J. A. C; Secomb, Sensors and sensing in biology and engineering., 399th Edition, Springer Berlin Heidelberg, New York, 2003.

[3] M. R. Maschmann, G. J. Ehlert, B. T. Dickinson, D. M. Phillips, C. W. Ray, G. W. Reich, J. W. Baur, Bioinspired Carbon Nanotube Fuzzy Fiber Hair Sensor for Air-Flow Detection, Advanced Materials 26 (20) (2014) 3230–3234. doi:10.1002/adma.201305285.
URL http://doi.wiley.com/10.1002/adma.201305285

[4] S. E. Bleckmann, H.; Mogdans, J.; Coombs, Flow Sensing in Air and Water., Springer-Verlag Berlin Heidelberg, 2014, pp. 197–213. doi:10.1007/978-3-642-41446-6.

[5] C. Magal, O. Dangles, P. Caparroy, J. Casas, Hair canopy of cricket sensory system tuned to predator signals, Journal of Theoretical Biology 241 (3) (2006) 459–466. doi:10.1016/j.jtbi.2005.12.009.
URL http://linkinghub.elsevier.com/retrieve/pii/S0022519305005412

[6] G. Crowley, L. Hall, Histological Observations on the Wing of the Grey-Headed Flying-Fox (Pteropus-Poliocephalus) (Chiroptera, Pteropodidae), Australian Journal of Zoology 42 (2) (1994) 215. doi:10.1071/ZO9940215.

[7] S. J. Sterbing-D'Angelo, C. F. Moss, Air Flow Sensing in Bats, Bleckmann, H., Mogdans, J., 2014, pp. 197–213. doi:10.1007/978-3-642-41446-6{_}8.

[8] T. Shimozawa, T. Kumagai, Y. Baba, Structural scaling and functional design of the cercal wind-receptor hairs of cricket, Journal of Comparative Physiology A 183 (2) 171–186. doi:10.1007/s003590050245.
URL http://dx.doi.org/10.1007/s003590050245

[9] B. T. Dickinson, J. R. Singler, B. A. Batten, Mathematical modeling and simulation of biologically inspired hair receptor arrays in laminar unsteady flow separation, Journal of Fluids and Structures 29 (2012) 1–17. doi:10.1016/j.jfluidstructs.2011.12.010.

[10] M. Luhar, H. M. Nepf, Flow-induced reconfiguration of buoyant and flexible aquatic vegetation (2011). doi:10.4319/lo.2011.56.6.2003.

[11] U. Brücker, C.; Rist, Complex Flow Detection by Fast Processing of Sensory Hair Arrays, Springer Berlin Heidelberg, Berlin Heidelberg, 2014.

[12] E. de Langre, Effects of Wind on Plants, Annual Review of Fluid Mechanics 40 (01) (2008) 141–168. doi:10.1146/annurev.fluid.40.111406.102135.

[13] A. Jana, A. Raman, B. Dhayal, S. L. Tripp, R. G. Reifenberger, Microcantilever mechanics in flowing viscous fluids, Applied Physics Letters 90 (11) (2007) 114110. doi:10.1063/1.2713238.

[14] P. J. Roache, Quantification of Uncertainty in Computational Fluid Dynamics, Annual Review of Fluid Mechanics 29 (1) (1997) 123–160. doi:10.1146/annurev.fluid.29.1.123.
URL http://www.annualreviews.org/doi/abs/10.1146/annurev.fluid.29.1.123

[15] D. J. Tritton, A note on vortex streets behind circular cylinders at low Reynolds numbers, Journal of Fluid Mechanics 45 (01) (1971) 203–208. doi:doi:10.1017/S0022112071003070.
URL http://dx.doi.org/10.1017/S0022112071003070